Article

Phase-Transformation-Activated MnCO$_3$ as Cathode Material of Aqueous Zinc-Ion Batteries

Funian Mo [1,*,†], Mangwei Cui [1,†], Liangliang Yang [1,†], Hao Lei [1], Sheng Chen [1], Jun Wei [1,*] and Litao Kang [2,*]

1   Shenzhen Key Laboratory of Flexible Printed Electronics Technology Center, School of Materials Science and Engineering, Harbin Institute of Technology, Shenzhen 518055, China
2   College of Environment and Materials Engineering, Yantai University, Yantai 264005, China
*   Correspondence: mofunian@hit.edu.cn (F.M.); junwei@hit.edu.cn (J.W.); kanglitao@ytu.edu.cn (L.K.)
†   These authors contributed equally to this work.

Abstract: The intrinsic high safety of rechargeable aqueous batteries makes them particularly advantageous in the field of large-scale energy storage. Among them, rechargeable Zn–Mn batteries with high energy density, low cost, high discharge voltage, and nontoxicity have been considered as one of the most promising aqueous battery systems. However, exiting research on manganese-based cathode materials mainly focuses on diverse manganese oxides analogs, while reports on other promising manganese-based analogs with high performance are still limited. Herein, we report a MnCO$_3$ cathode material, which can be manufactured on a large scale by a facile coprecipitation method. Interestingly, the MnCO$_3$ can spontaneously be converted into MnO$_2$ material during the charging process. The Zn–MnCO$_3$ battery delivers a highly specific capacity (280 mAh g^{-1}) even at the high current density of 50 mA g^{-1}. It is also noteworthy that the battery with a high loading mass (7.2 mg cm^{-2}) exhibits good reversibility of charge–discharge for 2000 cycles, showing a competitive cycling stability in aqueous systems.

Keywords: manganese-based material; phase transformation; zinc-ion batteries

1. Introduction

Lithium-ion batteries (LIBs) have dominated research on rechargeable battery systems. However, some persistent challenges still exist in LIBs such as limited metal Li resources, high cost, and environmental pollution. In particular, their potential safety problems are the main bottleneck in the current development [1–3]. Furthermore, the growing demand for wearable electronics and grid-scale energy storage continuously stimulates people's deeper exploration of other battery systems whose features include low price; safety; stability; excellent performance; long-life; and durability [4]. Among many metallic material-based batteries, Zinc (Zn) has attracted growing research interest due to its merits of high safety, abundant resources and low price, and it is usually identified as a promising anode material. Additionally, the Zn metal anode can offer high specific capacity (860 mAh g^{-1}) and relatively low redox potential (−0.76 V vs. SHE) [5–9]. Moreover, the aqueous ion battery possess the intrinsic advantage of high conductivity (1 S cm^{-1}), outperforming the nonaqueous ion battery (10^{-2} S cm^{-1}). The aqueous environment is also was beneficial for maintaining the safety and stability of the devices. Therefore, the aqueous zinc ion battery (AZIB) exhibits great potential as a promising candidate for a new generation of energy-storage equipment with economic applicability, safety, environmental protection, and excellent performance [10–18].

Manganese oxide (MnO$_2$) has been widely investigated and is considered an attractive energy-storage material due to its unique virtues of inexpensiveness, rich resources, environmental friendliness, non-toxicity, and multivariate mechanism of multi-valence (Mn, Mn^{2+}, Mn^{4+}, and Mn^{7+}, etc.) [19–21]. In recent years, MnO$_2$ with different crystal structures has been the most promising cathode material for aqueous zinc ion batteries [22]. For

instance, Kang et al. [23] proposed a novel aqueous energy-storage system called the zinc ion battery, which was made up of α-MnO_2, Zn, $ZnSO_4$ or Zn $(NO_3)_2$. The electrochemical reaction was realized on account of the migration of Zn^{2+} ions between the MnO_2 and Zn. Such a kind of rechargeable zinc–manganese (Zn–Mn) battery in a neutral or weak acid environment has attracted wide attention in the zinc battery community. In addition, Liu et al. [24] reported that adding manganese sulfate into an electrolyte solution could significantly suppress the dissolution of manganese-based cathodes materials into electrolytes in Zn–Mn batteries. Subsequently, these positive electrode materials were studied to varying degrees. Sun et al. [25] used the in situ electrodeposition of nano MnO_2 on carbon paper as the positive electrode of the battery. Wu et al. [26] used graphene to wrap α- MnO_2 nanowires as a battery cathode. Zhang et al. [27] studied β- MnO_2 as the cathode material of Zn–Mn batteries. However, apart from MnO_2, other Mn-based analogs have not received widespread attention in AZIB.

Manganese carbonate ($MnCO_3$) possesses a similar crystal structure to MnO_2 [28], reveling its potential as an electrode material. It has been widely investigated in the field of supercapacitors [29,30], which can realize a high voltage platform in alkaline electrolytes [31]. Normally, MnO_2 analogs are synthesized by the decomposition of manganese oxysalts and hydroxides. However, the process is particularly complex and energy-consuming. By contrast, $MnCO_3$ has many advantages, such as rich reserves, environmental friendliness, and easy synthesis. Moreover, its chemical properties are so active and stable that the charge transfer occurs in the process of phase transition, which provides a better cycle stability [28]. $MnCO_3$ is also widely used as an anode for LIBs [32]. Cao et al. [33] prepared the $MnCO_3$@rGO composite by anchoring $MnCO_3$ nanoparticles on rGO, which was used as a negative electrode of LIBs. Xie et al. [34] prepared the $MnCO_3$ microsphere and analyzed that the outstanding electrochemical performance was due to the transformation from micron particles to self-stabilized nanostructures during charging and discharging. However, reports on the applications of $MnCO_3$ are rarely seen in AZIBs, and the corresponding reaction mechanism involving the zinc-storage process and charge transfer needs further study.

In this work, we synthesized a micron particle $MnCO_3$ by the aqueous precipitation method. Interestingly, $MnCO_3$ can be converted into MnO_2 through a phase-change reaction. The Zn–$MnCO_3$ battery assembled in this way delivered a satisfactory specific capacity (280 mAh g^{-1}) at 50 mA g^{-1}. It is worth mentioning that under a high load (7.2 mg cm^{-2}), the battery can stably cycle for 2000 cycles.

2. Results

2.1. Structure Characterization Analysis of MnCO₃

The $MnCO_3$ micron particle was prepared using an aqueous precipitation method. The crystal structure of the as-synthesized sample was identified by using X-ray diffraction (XRD) technology. As shown in Figure 1, the diffraction peak of the prepared $MnCO_3$ was consistent with the standard card PDF#44-1472. The sharp diffraction peaks at 24, 25°, 31, 16°, 37, 52°, 41, 42°, and 45.18° correspond to the (012), (104), (110), (113), and (202) crystal planes, respectively, which prove that the prepared material is hexagonal $MnCO_3$. The better the crystallinity of $MnCO_3$, the sharper the peak. In addition, other weak peaks are observed in the XRD spectrum, which demonstrates the existence of Mn_3O_4 (PDF#18-0803).

The micro-morphology of $MnCO_3$ was systematically characterized by scanning electron microscope (SEM), transmission electron microscope (TEM), and high-resolution TEM (HRTEM) (Figure 2). It can be seen that the $MnCO_3$ is mainly composed of 2 μm spherical particles, and the enlarged SEM image (Figure 2b) shows that the micron-sized spherical $MnCO_3$ particles are composed of 20–30 nm small particles. In addition, the TEM image (Figure 2c) also proves that the prepared $MnCO_3$ is composed of nanoparticles. The high-resolution TEM imaging of $MnCO_3$ has been shown in Figure 2d. The TEM image reveals clear lattice fringes with an interplanar spacing of 0.288 nm, correlating to the (104) plane of $MnCO_3$. In addition, some results are placed in Supplementary Materials. The

N_2 adsorption/desorption isotherms (Figure S1a) illustrate that the specific surface area is 25.82 m^2/g, along with a mesoporous structure (Figure S1b).
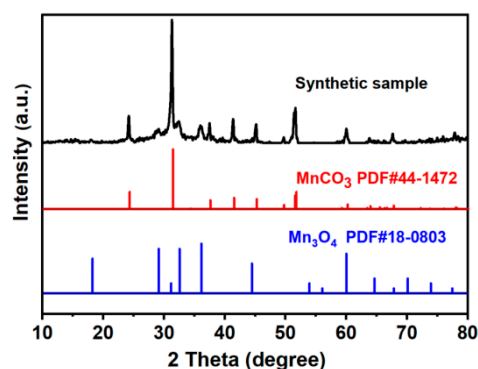
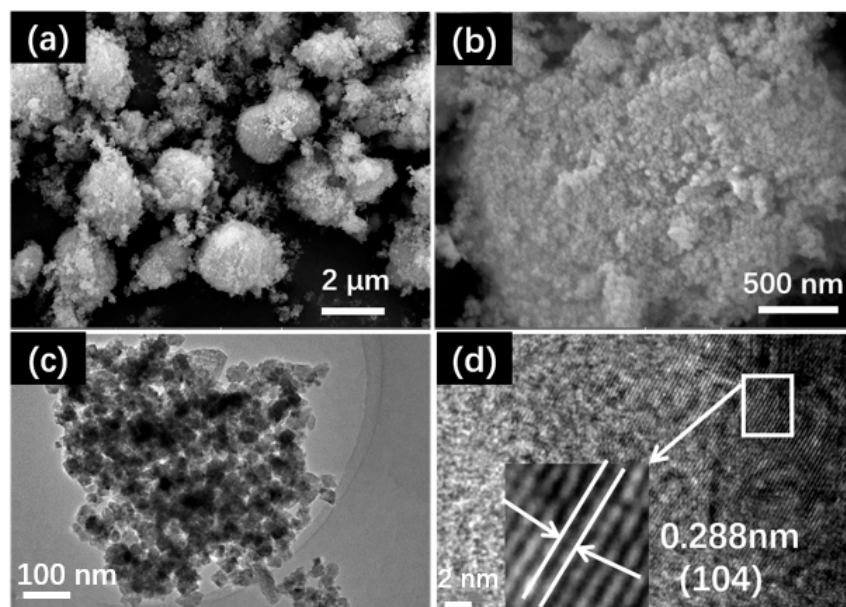

**Figure 1.** XRD patterns of the as-synthesized sample.

Figure 2. (**a**) SEM ×20k, (**b**) SEM ×100k, (**c**) TEM, and (**d**) HRTEM images of the surface morphology of $MnCO_3$.

2.2. Electrochemical Performance Analysis of $MnCO_3$

The $MnCO_3$ cathode was assembled in the 2032-coin cell with Zn foil and 3 M $ZnSO_4$ + 0.1 M $MnSO_4$, to evaluate its electrochemical performance. Figure 3a shows the cycling performance of the sample at low current density (50 mA g^{-1}). In the early cycle, the gradual increase of capacity is mainly the conversion of $MnCO_3$ to MnO_2, and the maximum capacity is reached only when the surface is completely converted to MnO_2. However, the poor performance of the low current cycling may be ascribed to the unstable structure of $MnCO_3$, which dissolves during cycling. The capacity of the battery exhibits a sharp decline after the initial increase, and the capacity is only 50 mAh g^{-1} at 100 cycles. Figure 3b shows the charge–discharge curves (50 mA g^{-1}) of the first three cycles of the battery. There is no capacity during the first discharge, indicating that the $MnCO_3$ sample will first undergo a charging reaction during the electrochemical reaction. The first charging platform is at 1.7 V, which corresponds to the Mn^{2+} in the electrolyte (Mn^{2+} may be provided by $MnCO_3$ solution in the subsequent process) deposited on the surface of $MnCO_3$ to form MnO_2. The subsequent corresponding charge–discharge curve platform is similar to the MnO_2 charge–discharge platform [35,36], which further verifies that MnO_2 is generated by the first charge. Meantime, the charge–discharge curves under different cycles show the

attenuation of capacity. It is worth mentioning that Mn_3O_4 exists in the synthetic materials. Although it will contribute to the capacity, it will be converted into MnO_2 in the subsequent charging and discharging. In addition, the mass of Mn_3O_4 was calculated for the specific capacity. Figure 3c shows the cycle performance of the sample under high current density (1 A g^{-1}). The first five times are 50 mA g^{-1}, which undergoes an activation process. The following test current density is 1 A g^{-1}, and the capacity retention still is 44.8% after 2000 cycles. Under a large current, the single-charge and discharge times become shorter, the precipitation rate of the $MnCO_3$ cathode is faster, and more crystals are generated, thus improving the structural stability of the electrode material to prevent its dissolution [37]. In addition, there are fewer side effects under high current density. Figure 4d shows the cycle performance under a high load (7.2 mg cm^{-2}) of 1 A g^{-1}; astonishingly, the specific capacity in the first cycles is 30 mAh^{-1}, and it shows a growing trend. The maximum specific capacity is reached 60 mAh g^{-1} after 100 cycles; then, the specific capacity declines, which is still 30 mAh g^{-1} after 2000 cycles.
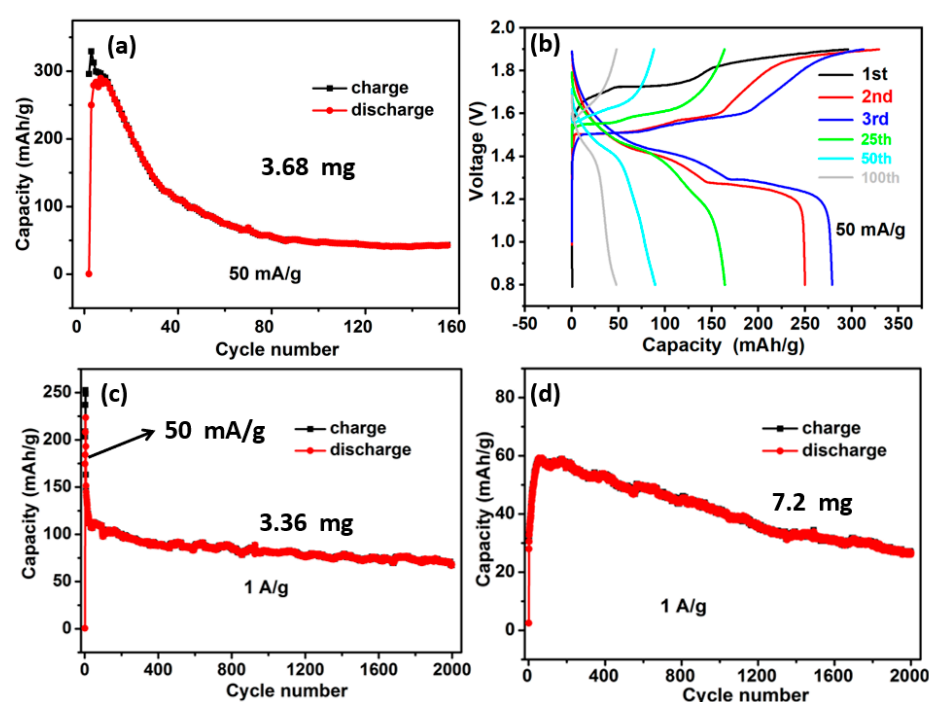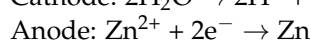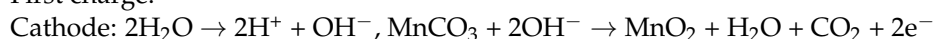

Figure 3. (**a**) The cycling performance at 50 mA g^{-1}; (**b**) charge/discharge curves of difference cycles at 50 mA g^{-1}; (**c**) the cycling performance at 1 A g^{-1}; and (**d**) the cycle performance under high load of 7.2 mg cm^{-2}.
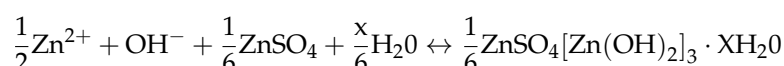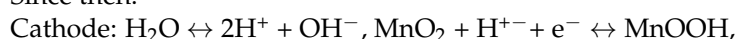
2.3. Reaction Mechanism Analysis

Based on the above-mentioned results, the possible electrode reactions of the $MnCO_3$–Zn battery system are proposed as shown below. During the first charging process, $MnCO_3$ is oxidized by OH^- to form MnO_2, and Zn^{2+} is reduced to form Zn. Therefore, the subsequent reaction mechanism is a typical Zn–MnO_2 battery, as follows:

First charge:

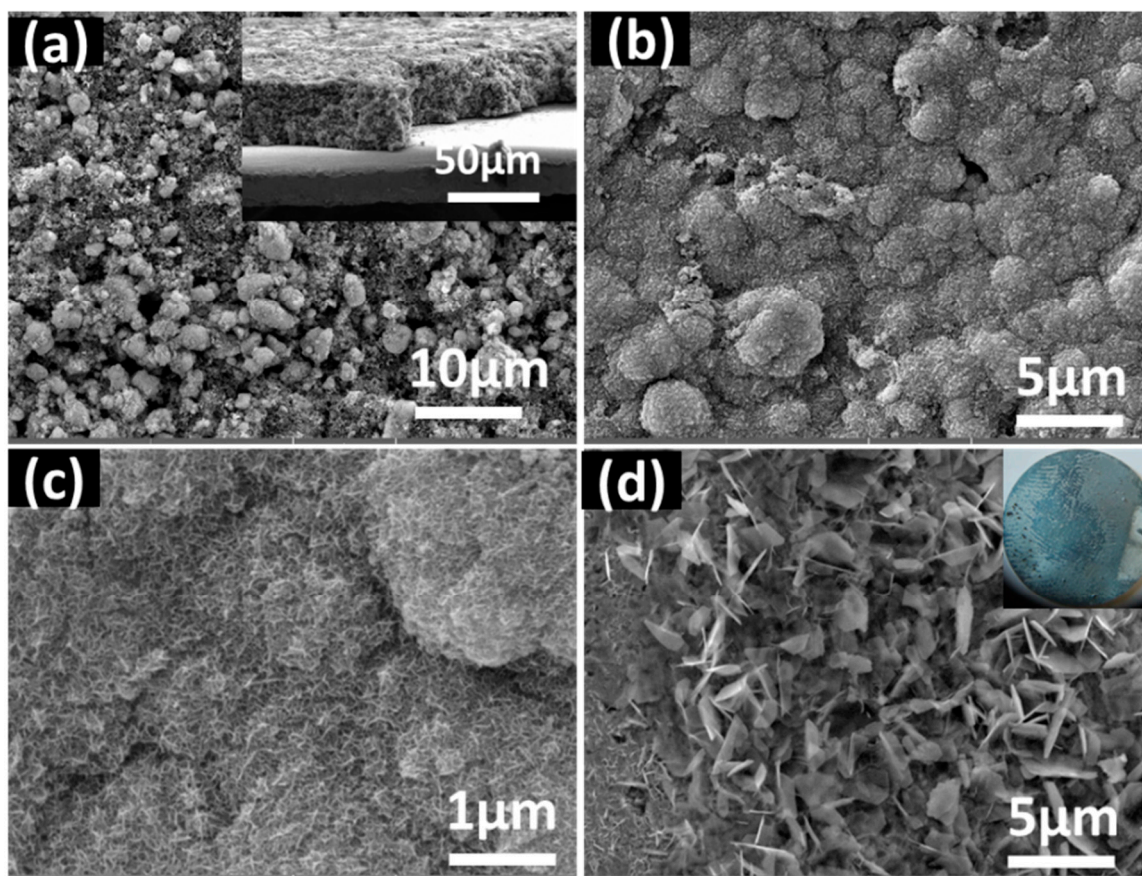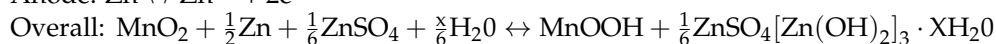Cathode: $2H_2O \rightarrow 2H^+ + OH^-$, $MnCO_3 + 2OH^- \rightarrow MnO_2 + H_2O + CO_2 + 2e^-$

Anode: $Zn^{2+} + 2e^- \rightarrow Zn$

Overall: $MnCO_3 + H_2O + ZnSO_4 \rightarrow MnO_2 + Zn + H_2SO_4 + CO_2$

Since then:

Cathode: $H_2O \leftrightarrow 2H^+ + OH^-$, $MnO_2 + H^+ + e^- \leftrightarrow MnOOH$,

$$\frac{1}{2}Zn^{2+} + OH^- + \frac{1}{6}ZnSO_4 + \frac{x}{6}H_2O \leftrightarrow \frac{1}{6}ZnSO_4[Zn(OH)_2]_3 \cdot XH_2O$$

Anode: $Zn \leftrightarrow Zn^{2+} + 2e^{-}$

Overall: $MnO_2 + \frac{1}{2}Zn + \frac{1}{6}ZnSO_4 + \frac{x}{6}H_2O \leftrightarrow MnOOH + \frac{1}{6}ZnSO_4[Zn(OH)_2]_3 \cdot XH_2O$
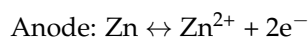

Figure 4. (**a**) SEM image of original $MnCO_3$ electrode (right corner: section image); (**b**) SEM of $MnCO_3$ electrode after first charge ×10k; (**c**) SEM of $MnCO_3$ electrode after first charge ×50k and (**d**) SEM of Zn electrode after first charge (right corner: digital image).

To verify the reaction mechanism, the following tests and characterization were carried out: during the first charge of the $MnCO_3$ electrode, bubbles were observed on the surface of the electrode material, which prove that CO_2 was generated during the oxidation of $MnCO_3$. Then, during the discharge, the bubbles disappeared (Figure S2). This corresponds to the reaction mechanism speculated by the first charge and discharge. At the same time, to better illustrate the oxidation of $MnCO_3$ into MnO_2 during the first charge, a non-aqueous electrolyte experiment was conducted for comparison (Figure S3). Unlike the aqueous electrolytes, it has almost no performance in the non-aqueous electrolyte, which proves that water must participate in the reaction (Figure S3b). The galvanostatic charge/discharge (GCD) test further shows that there is almost no capacity (Figure S3a). As shown in Figure S3c,d, the pH value of 3 M $ZnSO_4$ +0.1 M $MnSO_4$ is 4.122, and the pH of electrolyte after cycle is 3.791. By comparing the pH value of the electrolyte before and after charging and discharging, it also proves that a small amount of acid is generated in the electrolyte. This result is consistent with the proposed mechanism ($MnCO_3 + H_2O + ZnSO_4 \rightarrow MnO_2 + Zn + H_2SO_4 + CO_2$). In summary, the OH^{-} in the solution is provided by the aqueous solution, which further oxidizes $MnCO_3$ into MnO_2.

In addition, a series of SEM tests were performed to characterize the electrode materials after the GCD test. First, the morphology of the $MnCO_3$ electrode material was investigated by SEM (Figure 4a). The agglomerated nanoparticles are uniformly distributed on the surface of the electrode material. After the first charge, sheet-like substances are produced on the surface of the $MnCO_3$ electrode, and metal Zn sheets are produced

on the corresponding Zn foil surface (Figure 4b–d). As the number of cycles increases, $ZnSO_4[Zn(OH)_2]_3 \cdot xH_2O$ and MnOOH are continuously formed and converted on the electrode surface. During charging, $MnCO_3$ is gradually converted into MnO_2; MnOOH and sheet $ZnSO_4[Zn(OH)_2]_3 \cdot xH_2O$ are converted into MnO_2 and Zn, and it is a reverse process in the discharge process. $MnCO_3$ is gradually converted into MnOOH and sheet-like $ZnSO_4[Zn(OH)_2]_3 \cdot xH_2O$ (Figure S4).

To further verify the authenticity of the above products, the XRD after 5 cycles is shown in Figure 5. Except for the Ti substrate, the main product of the charging process is MnO_2, and the discharging product is $ZnSO_4[Zn(OH)_2]_3 \cdot xH_2O$. This also confirms that the proposed $MnCO_3$ is oxidized to MnO_2. In addition, a Mn_3O_4 peak with less obvious intensity is also found, which is mainly attributed to the heterophase produced by the synthesis of $MnCO_3$. However, the presence of MnOOH is not detected, which is contrary to the above inference. Liu et al. [24] reported that during the discharge process of Zn–MnO_2 batteries, the peak of MnOOH was submerged in the strong peaks from the carbon-paper current collector. This may explain why no obvious peak of MnOOH can be detected in Figure 5a.
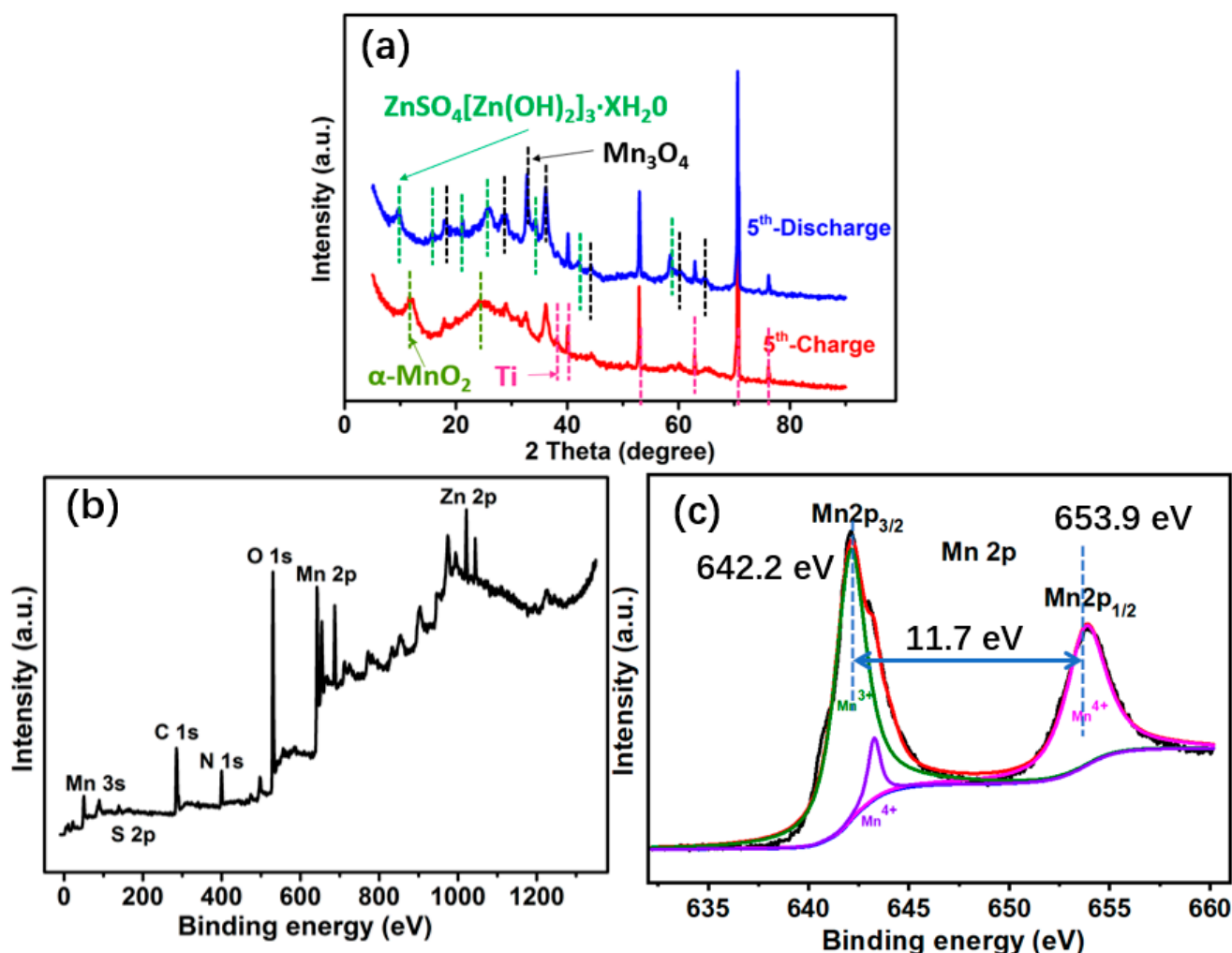
Figure 5. (**a**) XRD pattern of fifth charge and discharge of $MnCO_3$. XPS pattern of fifth charge of $MnCO_3$ (**b**) full spectra; (**c**) spectra of Mn 2p.

In addition, the XPS results further prove the above hypothesis. As shown in Figure 5b, Zn and Mn elements can be clearly detected in the electrode after the fifth charge. The binding energies positioned at 642.2 and 653.9 eV in the Mn 2p spectrum are derived from Mn $2p_{3/2}$ and S $2p_{1/2}$ of Mn^{4+}; the gap between the two peaks is 11.7 eV (Figure 5c). This

result is consistent with that reported by Chen et al. [38], which proves the existence of Mn^{4+}. Figure 6, Figures S5 and S6 show the EDS images of the $MnCO_3$ cathode after the fifth cycle. As shown in Figure 6, the element distribution after the charging state shows that the surface layer is mainly composed of Mn, and the bottom layer is mainly composed of C, which also shows that MnO_2 is covered on the surface of $MnCO_3$. The element distribution after the discharge state can be observed, and the discharge products contained more flake Zn element, indicating the formation of the $ZnSO_4$ $[Zn(OH)_2]_3$ and MnOOH phases.
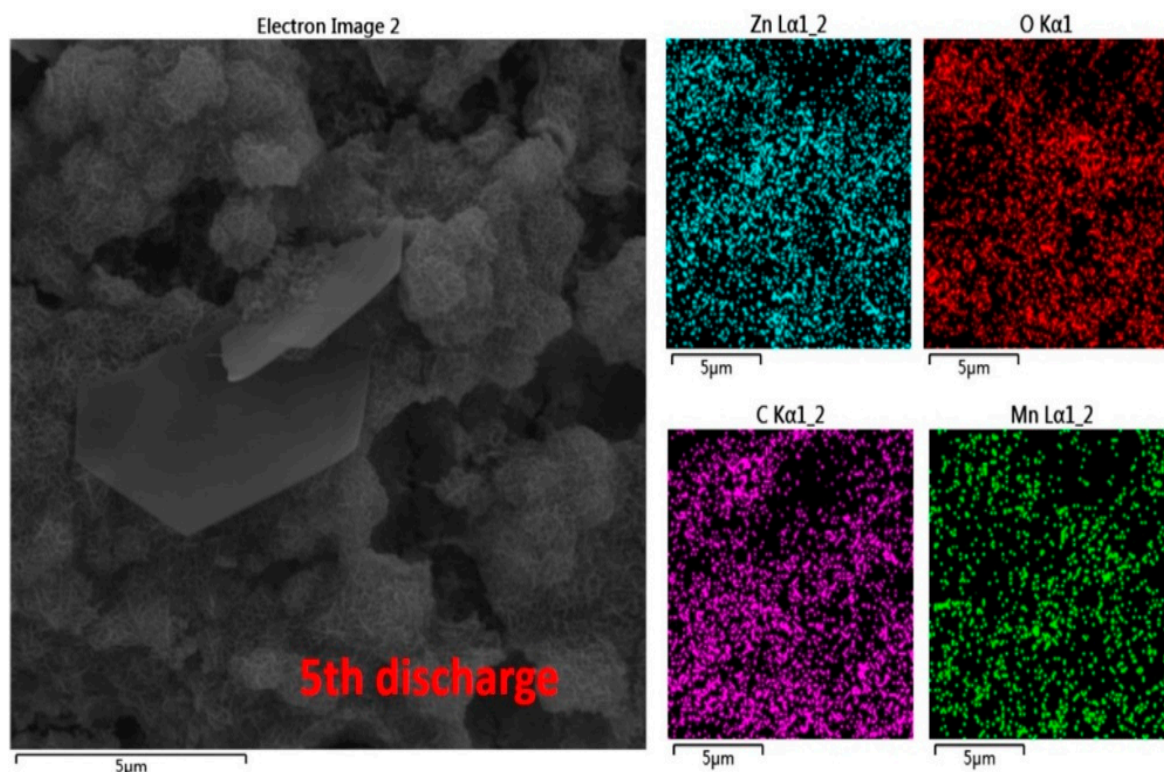
Figure 6. EDS of fifth discharge corresponding to $MnCO_3$ electrode.

3. Discussion

In summary, we developed a stable Zn–Mn battery based on the $MnCO_3$ electrode, which showed great potential in the development of manganese-based cathode materials. An interesting effect could be observed during the first few cycles: the $MnCO_3$ electrode underwent a phase-change reaction to convert into MnO_2, and the existence of MnO_2 was proved by SEM, XRD, XPS, and other different means. In addition, the appropriate reaction mechanism was generated. In short, the synthesis of the $MnCO_3$ material by a facile aqueous precipitation method could provide a new perspective on the large-scale manufacturing of manganese-based materials. Furthermore, under the condition of a high load and a large current, it could still maintain considerable capacity stability after 2000 cycles. This way of assembling batteries through phase-change conversion could provide a new research direction for more electrochemical research.

4. Materials and Methods

4.1. Procedures of $MnCO_3$ Preparation

$MnCO_3$ was synthesized by the aqueous precipitation method. First, 1.32 g of $MnSO_4$ was dissolved in 100 mL deionized water and 10 mL ethanol, and the resulting solution was marked as solution A. Second, 4.24 g of Na_2CO_3 was dissolved in 30 mL deionized water, called solution B. Then, solution A and solution B were mixed and magnetically stirred at

room temperature for 2 h. Finally, the resultant brown powder was washed with deionized water and ethanol, respectively, and the obtained brown powder was $MnCO_3$ powder.

4.2. Analysis and Characterization

The phase and crystal structure of the materials was performed by X-ray diffraction (XRD; D/Max-3B, Rigaku, Tokyo, Japan) using Cu Kα radiation ($\lambda = 0.154$ nm) at $10°$ min^{-1}. The morphology and element distribution of the products was shown by scanning electron microscopy (SEM; Mira3, Tescan), coupled with energy-dispersive X-ray spectroscopy (EDS; Oxford-Inca) and transmission electron microscopy (TEM; JEOL-2100F, 200 kV) with EDX detector. The elemental components and valence states of the samples were characterized by an X-ray photoelectron spectrometer (XPS, Kratos AXIS Ultra DLD-600W) using Al Kα radiation and Rex laboratory pH mete (PHSJ-6L). Nitrogen adsorption-desorption isotherms were collected by using ASAP2460.

4.3. Electrode-Preparation and Electrochemical-Performance Test

The electrode was provided by making a slurry of 80 wt.% of $MnCO_3$, 10 wt.% acetylene black, and 10 wt.% PVDF. After being fully mixed, N-methyl pyrrolidone (NMP) was added and ground for 30 min. The stirred slurry was cast onto titanium foil or a stainless-steel current collector. Finally, the electrode plates were dried at 60 °C for 12 h. The dried pole pieces were cut to a diameter of 16 mm, and the loading of $MnCO_3$ on each pole piece was between 3.0 and 7.2 mg cm^{-2}.

The pure metal zinc foil was used as an anode, and 3 M $ZnSO_4$ + 0.1 M $MnSO_4$ or 0.1 M $Zn(OTf)_2$ in dimethyl sulfoxide solution (DMSO) were utilized as electrolyte solutions. Glass fiber was selected to use as the separator, and the above materials were assembled into a 2032-coin battery (solubility: $MnCO_3-4.877 \times 10^{-5}$ g/100 mL, $MnSO_4-37.4$ g/100 mL).

The galvanostatic charge/discharge test was performed with a multichannel battery testing system (LAND CT2001A). Cyclic voltammetry (CV) was performed using a CHI660E electrochemical workstation.

Data Availability Statement: The data that support the findings of this study are available from the corresponding author upon reasonable request.

Conflicts of Interest: The authors declare no conflict of interest.

References

1. Ma, J.; Chen, B.; Wang, L.; Cui, G. Progress and prospect on failure mechanisms of solid-state lithium batteries. *J. Power Sources* **2018**, *392*, 94–115. [CrossRef]
2. Jacobson, M.Z. Review of solutions to global warming, air pollution, and energy security. *Energy Environ. Sci.* **2008**, *2*, 148–173. [CrossRef]
3. Durmus, Y.E.; Zhang, H.; Baakes, F.; Desmaizieres, G.; Hayun, H.; Yang, L.; Kolek, M.; Küpers, V.; Janek, J.; Mandler, D.; et al. Side by Side Battery Technologies with Lithium Ion Based Batteries. *Adv. Energy Mater.* **2020**, *10*, 2000089.
4. Wendy, P.; Jaime Andres, P.-T.; Alba, A. Tug-of-War in the Selection of Materials for Battery Technologies. *Batteries* **2022**, *8*, 105.
5. Shi, Y.; Chen, Y.; Shi, L.; Wang, K.; Wang, B.; Li, L.; Ma, Y.; Li, Y.; Sun, Z.; Ali, W.; et al. An Overview and Future Perspectives of Rechargeable Zinc Batteries. *Small* **2020**, *16*, 2000730. [CrossRef]
6. Tang, B.; Shan, L.; Liang, S.; Zhou, J. Issues and opportunities facing aqueous zinc-ion batteries. *Energy Environ. Sci.* **2019**, *12*, 3288–3304. [CrossRef]
7. Shang, W.; Yu, W.; Liu, Y.; Li, R.; Dai, Y.; Cheng, C.; Tan, P.; Ni, M. Rechargeable alkaline zinc batteries: Progress and challenges. *Energy Storage Mater.* **2020**, *31*, 44–57.
8. Parker, J.F.; Chervin, C.N.; Pala, I.R.; Machler, M.; Burz, M.F.; Long, J.W.; Rolison, D.R. Rechargeable nickel–3D zinc batteries: An energy-dense, safer alternative to lithium-ion. *Science* **2017**, *356*, 415–418. [CrossRef]
9. Wang, G.; Zhu, M.; Chen, G.; Qu, Z.; Kohn, B.; Scheler, U.; Chu, X.; Fu, Y.; Schmidt, O.G.; Feng, X. An Anode-Free Zn-Graphite Battery. *Adv. Mater.* **2022**, *34*, e2201957. [CrossRef]
10. Chen, Z.; Wang, P.; Ji, Z.; Wang, H.; Liu, J.; Wang, J.; Hu, M.; Huang, Y. High-Voltage Flexible Aqueous Zn-Ion Battery with Extremely Low Dropout Voltage and Super-Flat Platform. *Nano-Micro Lett.* **2020**, *12*, 75.
11. Cui, M.; Fei, J.; Mo, F.; Lei, H.; Huang, Y. Ultra-High-Capacity and Dendrite-Free Zinc–Sulfur Conversion Batteries Based on a Low-Cost Deep Eutectic Solvent. *ACS Appl. Mater. Interfaces* **2021**, *13*, 54981–54989. [PubMed]
12. Lei, H.; Cui, M.; Huang, Y. S-Doping Promotes Pyridine Nitrogen Conversion and Lattice Defects of Carbon Nitride to Enhance the Performance of Zn–Air Batteries. *ACS Appl. Mater. Interfaces* **2022**, *14*, 34793–34801. [CrossRef] [PubMed]
13. Cui, M.; Yan, B.; Mo, F.; Wang, X.; Huang, Y.; Fan, J.; Zhi, C.; Li, H. In-situ grown porous protective layers with high binding strength for stable Zn anodes. *Chem. Eng. J.* **2022**, *434*, 134688. [CrossRef]
14. Ling, W.; Yang, Q.; Mo, F.; Lei, H.; Wang, J.; Jiao, Y.; Qiu, Y.; Chen, T.; Huang, Y. An ultrahigh rate dendrite-free Zn metal deposition/striping enabled by silver nanowire aerogel with optimal atomic affinity with Zn. *Energy Storage Mater.* **2022**, *51*, 453–464. [CrossRef]
15. Song, J.; Xu, K.; Liu, N.; Reed, D.; Li, X. Crossroads in the renaissance of rechargeable aqueous zinc batteries. *Mater. Today* **2021**, *45*, 191–212.
16. Ma, L.; Chen, S.; Wang, D.; Yang, Q.; Mo, F.; Liang, G.; Li, N.; Zhang, H.; Zapien, J.A.; Zhi, C. Super Stretchable Zinc Air Batteries Based on an Alkaline Tolerant Dual Network Hydrogel Electrolyte. *Adv. Energy Mater.* **2019**, *9*, 1803046. [CrossRef]
17. Ming, F.; Zhu, Y.; Huang, G.; Emwas, A.H.; Liang, H.; Cui, Y.; Alshareef, H.N. Co-Solvent Electrolyte Engineering for Stable Anode-Free Zinc Metal Batteries. *J. Am. Chem. Soc.* **2022**, *144*, 7160–7170. [CrossRef]
18. Baishan, L. Transition Metal Dichalcogenides for High−Performance Aqueous Zinc Ion Batteries. *Batteries* **2022**, *8*, 62.
19. Bi, S.; Wang, S.; Yue, F.; Tie, Z.; Niu, Z. A rechargeable aqueous manganese-ion battery based on intercalation chemistry. *Nat. Commun.* **2021**, *12*, 6991.
20. Tian, H.; Li, Z.; Feng, G.; Yang, Z.; Fox, D.; Wang, M.; Zhou, H.; Zhai, L.; Kushima, A.; Du, Y.; et al. Stable, high-performance, dendrite-free, seawater-based aqueous batteries. *Nat. Commun.* **2021**, *12*, 237.
21. Lyubomir, S.; Delyana, M.; Violeta, K.; Antonia, S.; Radostina, S. Comparison of the Properties of Ni–Mn Hydroxides/Oxides with Ni–Mn Phosphates for the Purpose of Hybrid Supercapacitors. *Batteries* **2022**, *8*, 51.
22. Bi, S.; Zhang, Y.; Deng, S.; Tie, Z.; Niu, Z. Proton-Assisted Aqueous Manganese-Ion Battery Chemistry. *Angew. Chem. Int. Ed. Engl.* **2022**, *61*, e202200809. [CrossRef] [PubMed]
23. Xu, C.; Li, B.; Du, H.; Kang, F. Energetic Zinc Ion Chemistry: The Rechargeable Zinc Ion Battery. *Angew. Chem. Int. Ed.* **2011**, *51*, 933–935.
24. Pan, H.; Shao, Y.; Yan, P.; Cheng, Y.; Han, K.S.; Nie, Z.; Wang, C.; Yang, J.; Li, X.; Bhattacharya, P.; et al. Reversible aqueous zinc/manganese oxide energy storage from conversion reactions. *Nat. Energy* **2016**, *1*, 16039. [CrossRef]
25. Sun, W.; Wang, F.; Hou, S.; Yang, C.; Fan, X.; Ma, Z.; Gao, T.; Han, F.; Hu, R.; Zhu, M.; et al. Zn/MnO_2 Battery Chemistry With H^+ and Zn^{2+} Coinsertion. *J. Am. Chem. Soc.* **2017**, *139*, 9775–9778. [CrossRef]
26. Wu, B.; Zhang, G.; Yan, M.; Xiong, T.; He, P.; He, L.; Xu, X.; Mai, L. Graphene Scroll-Coated α-MnO_2 Nanowires as High-Performance Cathode Materials for Aqueous Zn-Ion Battery. *Small* **2018**, *14*, 1703850. [CrossRef]
27. Zhang, N.; Cheng, F.; Liu, J.; Wang, L.; Long, X.; Liu, X.; Li, F.; Chen, J. Rechargeable aqueous zinc-manganese dioxide batteries with high energy and power densities. *Nat. Commun.* **2017**, *8*, 405. [CrossRef]

28. Zheng, J.; Liu, P.; Yao, J.; Gan, Y.; Li, J.; Wang, C.; Liu, X.; Rao, Y.; Ma, G.; Lv, L.; et al. Phase transformation mechanism of MnCO$_3$ as cathode materials for aqueous zinc-ion batteries. *Front. Chem.* **2022**, *10*, 954592. [CrossRef]

29. Liu, D.; Hur, S.H.; Chung, J.S.; Choi, W.M. Fabrication of g-C$_3$N$_4$ Quantum Dots/MnCO$_3$ Nanocomposite on Carbon Cloth for Flexible Supercapacitor Electrode. *Appl. Sci.* **2020**, *10*, 7927. [CrossRef]

30. Karuppaiah, M.; Sakthivel, P.; Asaithambi, S.; Murugan, R.; Yuvakkumar, R.; Ravi, G. Formation of one dimensional nanorods with microsphere of MnCO$_3$ using Ag as dopant to enhance the performance of pseudocapacitors. *Mater. Chem. Phys.* **2019**, *228*, 1–8.

31. Lv, Y.; Dong, G.; Kang, J.; Han, W.; Li, L. MnF$_2$-Ni and MnCO$_3$-Ni derived from the same raw materials for high-performance supercapacitor. *Mater. Lett.* **2018**, *215*, 125–128. [CrossRef]

32. Zhang, R.; Wang, D.; Qin, L.; Wen, G.; Pan, H.; Zhang, Y.; Tian, N.; Zhou, Y.; Huang, X. MnCO$_3$/Mn$_3$O$_4$/reduced graphene oxide ternary anode materials for lithium-ion batteries: Facile green synthesis and enhanced electrochemical performance. *J. Mater. Chem. A* **2017**, *5*, 17001–17011.

33. Zhou, L.; Kong, X.; Gao, M.; Lian, F.; Li, B.; Zhou, Z.; Cao, H. Hydrothermal Fabrication of MnCO$_3$@rGO Composite as an Anode Material for High-Performance Lithium Ion Batteries. *Inorg. Chem.* **2014**, *53*, 9228–9234. [PubMed]

34. Xiao, L.; Wang, S.; Wang, Y.; Meng, W.; Deng, B.; Qu, D.; Xie, Z.; Liu, J. High-Capacity and Self-Stabilized Manganese Carbonate Microspheres as Anode Material for Lithium-Ion Batteries. *ACS Appl. Mater. Interfaces* **2016**, *8*, 25369–25378.

35. Alfaruqi, M.H.; Gim, J.; Kim, S.; Song, J.; Jo, J.; Kim, S.; Mathew, V.; Kim, J. Enhanced reversible divalent zinc storage in a structurally stable α-MnO$_2$ nanorod electrode. *J. Power Sources* **2015**, *288*, 320–327. [CrossRef]

36. Qiu, W.; Li, Y.; You, A.; Zhang, Z.; Li, G.; Lu, X.; Tong, Y. High-performance flexible quasi-solid-state Zn–MnO$_2$ battery based on MnO$_2$ nanorod arrays coated 3D porous nitrogen-doped carbon cloth. *J. Mater. Chem. A* **2017**, *5*, 14838–14846. [CrossRef]

37. Zhou, J.; Dong, A.; Du, L.; Yang, C.; Ye, L.; Wang, X.; Zhao, L.; Jiang, Q. Mn-Doped ZnO Microspheres as Cathode Materials for Aqueous Zinc Ion Batteries with Ultrastability up to 10 000 Cycles at A Large Current Density. *Chem. Eng. J.* **2020**, *421*, 127770.

38. Chen, Y.; Qin, W.; Wang, J.; Chen, B. Fabrication and electrochemical performance of nanoflake MnO$_2$@carbon fiber coaxial nanocables for supercapacitors. *J. Appl. Electrochem.* **2015**, *46*, 241–249. [CrossRef]